# Edge displacement scores

**Arne Melsom**[1]

[1]Norwegian Meteorological Institute, Oslo, Norway

**Key Points:**

- A new algorithm for quantifying the quality of model results for displacement of the sea ice edge is introduced
- The algorithm has been applied comparing two years of model results for sea ice in the Barents Sea with observations
- The algorithm may also be used more generally to check the quality of displacements of the perimeter of binary fields

Corresponding author: Arne Melsom, arne.melsom@met.no

**Abstract**

As a consequence of a diminishing sea ice cover in the Arctic, activity is on the rise. The position of the sea ice edge, which is generally taken to define the extent of the ice cover, changes in response to dynamic and thermodynamic processes. Forecasts for sea ice expansion due to an advancing ice edge will provide information that can be of significance for operations in polar regions. However, the value of this information depends on the quality of the forecasts. Here, we present methods for examining the quality of forecasted sea ice expansion and the geographic location where the largest expansion are expected from the forecast results. The algorithm is simple to implement, and an examination of two years of model results and accompanying observations demonstrates the usefulness of the analysis.

## Plain Language Summary

As sea ice is retreating in the Arctic due to climate change, large areas are becoming open for commercial shipping, harvesting of resources and other activities in the high north. Nevertheless, sea ice will remain a challenge to such activities in decades to come. To this end, forecasting changes in the sea ice extent will become increasingly important. And, like any forecast, their use must be backed up by assessments of their quality. Here a new method is proposed that will provide information of the quality of forecasts for the motion of the sea ice edge.

## 1 Introduction

Due to climate change the sea ice extent is in decline in the Arctic (Parkinson, 2014). This change has led to increased activity in the region, and commercial shipping in open waters via Arctic sea routes will become increasingly economically viable in the 21$^{\text{st}}$ century (Aksenov et al., 2017). Thus, products for monitoring and forecasting sea ice conditions are receiving growing attention.

The past years have seen a flurry of activity related to assessing the quality of sea ice products. Dukhovskoy et al. (2015) present a review and comparison of various traditional metrics for assessments of the skill of sea ice models. Goessling et al. (2016) introduce the Integrated Ice-Edge Error (IIEE), a quantity for describing mismatching sea ice extents from two products, in their examination of the predictability of the sea ice edge. Melsom et al. (2019) took advantage of the IIEE in their examination of various metrics for assessment of the quality of forecasts for the sea ice edge position. Methods for examining the quality of probabilistic results for sea ice conditions have been introduced by Goessling and Jung (2018) and Palerme et al. (2019). Recently, Cheng et al. (2020) have examined the accuracy of a visually estimated ice concentrations monitoring product.

The changing position of the sea ice edge is generally not only shifted by dynamic advection, but can be significantly affected by the thermodynamics as well (Bitz et al., 2005). Thus, the temporal displacement of the sea ice edge will be affected by freezing along the perimeter of the sea ice extent in winter, and melting in summer. Hence, pattern-recognition algorithms for displacements using maximum cross-correlation (MCC) methods such as those introduced by Leese et al. (1971) for wind vectors, and later for ocean surface currents (Tokmakian et al., 1990) and sea ice vectors (Lavergne et al., 2010), are not ideal for tracking displacements of the sea ice edge.

Ebert and McBride (2000) examined the position error of the contiguous rain area in weather forecasts. They determined the error vector from a total squared error minimization method when shifting the forecasted rain region to match the corresponding observations. Their preference of applying an error minimization algorithm rather than an MCC approach was motivated by the former having better representations of displacement of rainfall maxima. Displacement of the perimeter of the contiguous rain area was not addressed in their investigation.

We begin this study by presenting a new algorithm for assessing the quality of representations of the sea ice edge by comparing results for two different products. This is described in section 2, where issues related to sea ice emerging in the vicinity of boundaries are also addressed. Next, in section 3 we apply the algorithm in an examination of displacements of the sea ice edge in the Barents Sea in a model product, and compare the results to data from an observational product. Finally, we provide our concluding remarks in section 4.

## 2 Methods

In order to illustrate the validation metrics that are introduced in this section, some idealized distributions are introduced, as depicted in Figure 1. The domain is divided into $1000 \times 500$ square grid cells, and we set the length of the side of a grid cell to 1. Denote the line that separates regions with binary values 0 and 1 as an edge line, and let $L^{(o)}(t)$ and $L^{(m)}(t)$ denote observed and modeled edges, respectively, at time $t$. Idealized examples with edges for $L^{(o)}$ and $L^{(m)}$ at two different times, $t_0$ and $t_0{+}\Delta t$, are displayed. In the context of forecasting, $L^{(m)}(t_0)$ may be taken to represent the model initialization at $t_0$ and $L^{(m)}(t_0{+}\Delta t)$ is then the forecast at a temporal range of $\Delta t$. The other binary fields can represent observations at the same times.

### 2.1 Single product metrics

We aim at defining metrics that describe differences in maximum edge displacements between two products. In order to do so, we must first introduce a quantity that properly measures the maximum displacement in one product. Here a definition is provided which is a gridded, signed, one-sided variation of the Hausdorff distance (Dukhovskoy et al., 2015).

For the remainder of this investigation we will take the binary fields to be representations of sea ice, with values assigned to 0 and 1 for conditions of no ice and ice, respectively. We will here associate the presence of ice (value 1) with sea ice concentration $c$ exceeding $c_{edge} = 0.15$. In a gridded representation the ice edge can then be taken to be constituted by the grid cells $e = [i, j]$ that meet the condition

$$c[i,j]{\geq}c_{edge} \quad \wedge \quad \min\big(c[i-1,j], c[i+1,j], c[i,j-1], c[i,j+1]\big) < c_{edge} \tag{1}$$

where $\wedge$ is the logical AND operator. Denoting the N grid cells that satisfy this condition by $e_1, e_2, \ldots, e_N$ the ice edge is then the line

$$L = \{e_1, e_2, \ldots, e_N\} \tag{2}$$

This follows the algorithm presented in Melsom et al. (2019). Let $L^{(1)}, L^{(2)}$ denote the sea ice edges for two representations of the sea ice cover. Furthermore, let $d_n^{2:1}$ be the displacement distance between grid node $e_n^{(2)}$ in $L^{(2)}$ and line $L^{(1)}$, *i.e.*,

$$d_n^{2:1} = s \min ||e_n^{(2)} - L^{(1)}|| \tag{3}$$

where $s$ is +1 or -1 when $e_n^{(2)}$ is on the no ice or ice side of $L^{(1)}$, respectively, i.e., $s$ is +1 if $c[e_n^{(2)}]^{(1)} < c_{edge}$ and -1 if $c[e_n^{(2)}]^{(1)}{\geq}c_{edge}$ ($c[e]^{(1)}$ is the sea ice concentration for grid cell $e$ for the representation with an ice edge given by $L^{(1)}$). Here, $||z||$ is the Euclidean distance of $z$. We can now introduce the maximum distance as

$$d_{max}^{2:1} = \max(d_n^{2:1}) \tag{4}$$

Note that the definition of the sign $s$ in equation 3 has been chosen so that equation 4 will return the largest positive value among $d_n^{2:1}$. If all values of $d_n^{2:1}$ are negative, the result is the distance with the lowest magnitude. The definition of $s$ was designed so that $d_{max}^{2:1}$ will represent the displacement of the largest sea ice advance from $L^{(1)}$ to $L^{(2)}$. For reference, we note that the Hausdorff distance $d_H$ between lines $L^{(2)}$ and $L^{(1)}$ is

$$d_H = max(|d_n^{2:1}|, |d_m^{1:2}|) \tag{5}$$

see e.g. Dukhovskoy et al. (2015).

So far, we have restricted the analysis to consider the maximum displacement. However, it is of interest to examine more generally the displacement distance between $L^{(2)}$ and $L^{(1)}$. In addition to a visual inspection that can be done by looking at a graphical presentation (see Figure 1 for examples), we can consider all values for $d_n^{2:1}$ and summarize the distribution in a table with a suitable definition of distance categories, or present the distribution as e.g. a cumulative probability distribution. A table for selected distance categories for the idealized model results displayed in Figure 1 is given as Table S1 in the supporting information. We find that in this case, $d_{max}^{m(t_0+\Delta t):m(t_0)} = 113.2$ (the distance between the red and light red diamonds in the figure), while $d_{max}^{o(t_0+\Delta t):o(t_0)} = 97.9$ (the distance between the black and gray full circles).

To avoid inflating the sample size when time series results are examined, one may consider subsampling at the spatial decorrelation length along the ice edge. For the distribution of $d_n^{2:1}$ a proper decorrelation length can be computed if the edge nodes $e_n^{(2)}$ are in sequence along $L^{(2)}$.

Also, when a time series of results is examined, the distribution of $d_{max}^{2:1}(t)$ can be examined analogously to results for $d_n^{2:1}$. We will show results for $d_{max}^{2:1}(t)$ when comparing model results and observations in the case study that is undertaken in section 3.

### 2.2 Two-product metrics

The main purpose of the work presented here is to define metrics that can contribute in an evaluation of the quality of model forecasts when complementary observations are available. Consequently, binary fields that are taken to represent observations as well as model results are introduced, as displayed in Figure 1.

A useful initial evaluation of how model results for displacement and the corresponding observational data compare, is to inspect their cumulative distributions. These distributions are displayed for the idealized example in Figure 2. We note that the shapes of the cumulative distributions are similar, with model displacements shifted approximately 20 grid units higher for the entire distribution.

From the perspective of an observer, a useful property is the quality of the forecasted maximum displacement of the binary field, over the forecast period. A simple quantity that provides relevant information, is the difference in the maximum displacement as given by equation 4, *i.e.*,

$$\Delta d_{max}^{2:1} = \max(d_i^{m2:m1}) - \max(d_j^{o2:o1}) \tag{6}$$

where $o1, o2$ are observed ice edges at $t_0$ and $t_0+\Delta t$, respectively (black and gray lines in Figure 1), and $m1, m2$ are the corresponding model results. From the results for the idealized example that was introduced in section 2.1 above the model is over-estimating the maximum displacement, by $\Delta d_{max}^{2:1} = 15.3$ grid cell units.

A similar quantity that provides site specific information is the local difference in displacement of the model binary field where the maximum value is found in the observations. Let $e_0^{o2}$ be the position in $L^{(o2)}$ to which the maximum edge displacement is found in the observations. Then, determine $\epsilon_0^{m2}$, the edge grid cell closest position of the model edge at the same time. In Figure 1, the positions $e_0^{o2}$ and $\epsilon_0^{m2}$ are indicated by the full black and full red circles, respectively. Following equation 3 the corresponding local edge displacement in the model results is

$$\delta_0^{m2:m1} = s \min ||\epsilon_0^{m2} - L^{(m1)}|| \tag{7}$$

where $L^{(m1)} = L^{(m)}(t_0)$. For the idealized example, we find that $\delta_0^{m2:m1} = 83.9$. The local difference in displacement between model and observations, with reference to the position $e_0^{o2}$, becomes

$$\Delta\delta_{max}^{2:1} = \delta_0^{m2:m1} - \max(d_n^{o2:o1}) \tag{8}$$

so, for the idealized example we have $\Delta\delta_{max}^{2:1} = -14$, *i.e.* a local underestimation of the displacement in the model results.

One aspect which is not disclosed by the metrics introduced thus far, is to what degree forecasts manage to reproduce the geographical location of the observed maximum displacements. In order examine such a relation, we first compute the decorrelation length of displacements given by equation 3. If we denote this grid distance by $\Delta n$, we restrict the analysis of grid cells and corresponding displacements to

$$\{\ldots, \epsilon_{0-2\Delta n}^{m2}, \epsilon_{0-\Delta n}^{m2}, \quad \epsilon_{0+\Delta n}^{m2}, \epsilon_{0+2\Delta n}^{m2}, \ldots\}, \tag{9}$$

$$\{\ldots, \delta_{0-2\Delta n}^{m2:m1}, \delta_{0-\Delta n}^{m2:m1}, \quad \delta_{0+\Delta n}^{m2:m1}, \delta_{0+2\Delta n}^{m2:m1}, \ldots\} \tag{10}$$

respectively, limited by the first and last nodes along the line $L^{(m2)}$. Next, we construct bins analogously to the method used for producing rank histograms (Talagrand diagrams) for ensemble forecasts (Hamill, 2001): First, distances listed in equation 10 are sorted by increasing values, and then bins are introduced for values smaller than the minimum distance, the intervals between the sorted distances, and for values larger than the maximum distance. The bin placement of $\delta_0^{m2:m1}$ then gives the rank of this displacement.

In the present idealized example we find that $\Delta n = 42$, and the rank of $\delta_0^{m2:m1}$ in the 24 resulting bins is 9. When multiple forecasts are examined, the decorrelation length will generally change, as will the length of the edges. Thus, in order to derive a meaningful statistic quantity we subsample a fixed sized random set of grid cells from equation 10, and an analysis of the ranks of displacement distances can be performed.

For the idealized example, a set of nine randomly subsampled edge positions from those given by equation 9 for the model results at $t = t_0 + \Delta t$ is displayed by open circles in Figure 1. For this particular case, in the range from 1 to 10 the rank of the displacement $\delta_0^{m2:m1}$ is 3.

### 2.3 Open boundaries and coasts

Sea ice products may be regional, having one or more boundaries along which the domain is connected to the surrounding area along open ocean boundaries. In that case, sea ice may be advected into the product domain across an open boundary, and the algorithm as given in section 2.1 should be modified in order to avoid misinterpretations of results for displacement distances that may arise. An illustrative case will be discussed in section 3.

First, set the open boundary grid lines as

$$L^{OB} = \{e_{1_{OB}}, e_{2_{OB}}, \ldots, e_{N_{OB}}\} \tag{11}$$

where $e_{n_{OB}}$ is any ocean grid cell along the boundary of the domain. Then $L^{(1)}$ can be replaced by

$$\tilde{L}^{(1)} = L^{(1)} \cup L^{OB} \tag{12}$$

and for the corresponding distances we introduce the notation $\tilde{d}$, so e.g. Equation 3 is written

$$\tilde{d}_i^{\,2:1} = j \min ||e_i^{(2)} - \tilde{L}^{(1)}|| \tag{13}$$

It must be noted that if the ice is imported into the domain, the distances $\tilde{d}$ associated with such a displacement will be underestimated, since the real position of the ice edge outside of the analysis domain at $t_0$ is unknown.

Similarly, there can be cases where freezing of ice occurs along the coastline, e.g. due to colder air in the vicinity of continents, or less salty water masses close to the coastline. This is another case where the algorithm above can yield grossly exaggerated displacement distances. Again, the problem can be overcome by including additional grid lines.

Set the coastal grid lines as

$$L^C = \{e_{1_C}, e_{2_C}, \ldots, e_{N_C}\} \tag{14}$$

where $e_{n_C}$ is any ocean grid cell along the coastline. Then $L^{(1)}$ can be replaced by

$$\overline{L}^{(1)} = L^{(1)} \cup L^C \tag{15}$$

For a regional model, the typical situation is that there are both open boundaries and coastlines. In that case, we may combine the above modifications of the algorithm by adopting

$$\tilde{\overline{L}}^{(1)} = L^{(1)} \cup L^{OB} \cup L^C \tag{16}$$

## 3 A case study

To illustrate the methodology introduced in section 2, we examine model results from a coupled ocean – sea ice model, and compare with relevant observational data. The model results are taken from the SVIM hindcast archive (SVIM, 2015). For the present illustrative purpose we limit the analysis to the two year period 2000-01-01 – 2001-12-31. Results are available as daily means on the model configuration's native 4 km stereographic grid projection (Lien et al., 2013).

The ocean module of the coupled model used for the regional simulation is the Regional Ocean Modeling System (ROMS), described in Haidvogel et al. (2008) and references therein. The sea ice module was developed by Budgell (2005). The ice model dynamics are based on the elastic-viscous-plastic (EVP) rheology after Hunke and Dukowicz (1997) and Hunke (2001), and the ice thermodynamics are based on Mellor and Kantha (1989) and Häkkinen and Mellor (1992).

The model results for sea ice concentration are somewhat noisy on the grid cell scale, owing to the dispersiveness of the numerical scheme. In some regions, the grid cells that constitute the ice edge as defined by equation 1 can then appear as a mesh-like collection of cells. In order to reduce the impact of this issue, we applied the second order checkerboard suppression algorithm (Li et al., 2001) to the model results before conducting the present analysis.

We compare model results with observations from the Arctic Ocean Sea Ice Concentration Charts *Svalbard* which is a multi-sensor product that uses data from Synthetic Aperture Radar (SAR) instruments as its primary source of information (WMO, 2017). This product covers the northern Nordic Seas, the Barents Sea and adjacent ocean regions. It is available on a stereographic grid projection with a resolution of 1 km. The product will be referred to as the ice chart data hereafter. Data availability is restricted to working days. During a regular week, we then have four days with 24 h displacement results. The data set is also slightly reduced due to holidays, and a total of 354 days with 24 h ice edge displacement results were available from the present two year period.

The present study will be restricted to results and data for the Barents Sea. The SVIM simulation domain is displayed in Figure S1 (supporting information), where the Barents Sea analysis region is highlighted. Ice chart results are integrated onto the SVIM domain, and all grid cells inside the Barents Sea region that become dry in either product are masked prior to the analysis. The analysis region is then constituted by 80.399 wet grid cells, which represent an area of $1.29 \cdot 10^6\,\mathrm{km}^2$.

We first examine the distribution of daily maximum ice edge displacements. The results are summarized in Table 1, where results from the 354 days with 24 h displacements from both products have been included. We note that about 2/3 of the displacements in model results are in the range $10 - 30$ km. The corresponding distribution of results from the ice chart data has two maxima, one for the range $20 - 40$ km which accounts for nearly half of the cases, and a secondary maximum for short ($0 - 10$ km) displacements. The averages of the daily maximum displacement distances are 25 km and 36 km for the SVIM results and the ice chart data, respectively.

The category distributions in Table 1 change only moderately when the algorithm for computing displacements are modified as described in section 2.3. However, in a few cases the results from the general algorithm given in section 2.1 do not properly describe true displacements. To illustrate this, we have selected a case where the two approaches give diverging results: the change in the ice edge position from 2001-10-23 to 2001-10-24, as displayed in Figure S2 in the supporting information.

This is a case where sea ice is displaced into the analysis region across the northern boundary. The example demonstrates that in such cases, the general algorithm in section 2.1 gives unreasonable results: The maximum displacement of 285 km that emerges from the algorithm is indicated by a black line. The maximum distance using the modified algorithm in section 2.3 is 79 km (red line).

For the examination of the degree to which SVIM results reproduce the geographical location of the observed maximum displacement, nine values were chosen randomly from each set of 24 h results emanating from equation 10. Moreover, the requirement of at least nine additional ice edge positions separated by the decorrelation length scale restricts the cases that can be considered in this analysis. Thus, from the full set of 354 cases with 24 h displacement results, 235 cases were kept in the analysis of ranked displacements.

The resulting frequency distribution for each of the ten ranks is displayed as gray vertical bars in Figure 3, with rank values from 0 to 9. The highest rank (9) results when the model displacement close to the site with maximum displacement in the observations (the reference displacement, $\delta_0^{m2:m1}$) is larger than all displacements from the nine subsampled ice edge positions. The next rank (8) corresponds to cases where one and only one of the subsampled positions have a larger displacement than the reference displacement, and so on. In other words, high ranks indicate situations in which the position of the maximum displacement is described with a relatively high quality.

The expected average rank from a model with no quality in reproducing the position of the maximum ice edge displacement is 4.5, with half of the cases with a rank in the range $0 - 4$, and the other half in the range $5 - 9$. In the analysis of the results from the SVIM archive, we find that 35% of the cases have rankings in the range $0 - 4$, while 65% have rankings in the range $5 - 9$.

Furthermore, the average rank in the present analysis is 5.5. For a random distribution of 235 integer numbers in the range $0$ –$9$ the $0.005^{\mathrm{th}}$ and $0.995^{\mathrm{th}}$ percentiles are 4.015 and 4.985, respectively. Thus, the analysis reveals that while the model results are far from perfect, the average ranking of 5.5 is significantly higher than results from random spatial distributions of ice edge displacements.

## 4 Concluding remarks

We present a simple algorithm for examination of the displacement of the edge (or the front) of a binary field. This forms the basis for a subsequent analysis of statistical properties for such displacements. Furthermore, additional methods have been introduced for the purpose of comparing two different products that are available as descriptions of the same situation.

The present study has been framed in the context of results for displacements of the sea ice edge. Thus, the case study which was investigated in section 3 was based on data for the sea ice edge from satellite observations, and simulation results from a coupled ocean – sea ice model. However, the algorithm that was introduced in section 2 can be applied to the displacement of the perimeter of any property that can be represented by a continuous binary field. Stratiform precipitation is an example of another property for which the present methods are relevant.

Note that we have used the term *displacement* rather than *advection*. The reason for this is that displacements need not be purely of an advective nature. In the case of sea ice, the displacement of the initial edge will generally be affected by freezing or melting along the perimeter of the sea ice extent. Analogously, displacement of the area affected by stratiform precipitation can be affected by new condensation or partial depletion of the cloud.

As demonstrated in the example depicted in Figure S2 (supporting information), the original algorithm described in section 2.1 and 2.2 may yield results that represent other aspects than true displacements. Here, we have amended situations in which the sea ice enters a limited area domain across an open model domain boundary, and situations where freezing takes place next to a physical boundary (the coast). The corresponding simple modifications of the algorithm that was introduced in section 2.3 eliminates such issues, as revealed from the sample situation in Figure S2.

However, there may be other issues that can distort results that are produced by the present analysis. One example is cases where features are seen to arise seemingly spontaneous from one time of analysis to another: The algorithm in section 2 can e.g., if applied to precipitation data, give rise to unrealistic results for displacements when convective precipitation cells become established.

Results from the algorithms that are introduced in the present study give valuable information regarding the changing extent of sea ice, and how well the displacement of the observed and modeled sea ice edge agree. These algorithms have proven to provide simple, yet robust and informative assessments for the quality of ice edge forecasts both with respect to the largest displacements from one time to another as well as with respect to the reproduction of the geographical position where the largest displacement occurs.

**Acknowledgments**
This study was performed within the Nansen Legacy project on behalf of the Norwegian Research Council, funded under contract no. 276730. Supporting funding was provided by the Copernicus Marine Environmental and Monitoring Service under Mercator Océan from contract no. 2015/S 009-011301. Model results that were analyzed are available from `https://archive.norstore.no/pages/public/datasetDetail.jsf?id=10.11582/2015.00014`, while the observations are available from `https://thredds.met.no/thredds/`

catalog/arcticdata/met.no/iceChartSat/catalog.html. All figures were created using the NCAR Command Language (NCL, 2019).

## References


Aksenov, Y., Popova, E. E., Yool, A., Nurser, A. G., Williams, T. D., Bertino, L., & Bergh, J. (2017). On the future navigability of arctic sea routes: High-resolution projections of the arctic ocean and sea ice. *Mar. Policy*, *75*, 300–317. doi: 10.1016/j.marpol.2015.12.027

Bitz, C. M., Holland, M. M., Hunke, E. C., & Moritz, R. E. (2005). Maintenance of the sea-ice edge. *J. Clim.*, *18*(15), 2903–2921. doi: 10.1175/JCLI3428.1

Budgell, P. W. (2005). Numerical simulation of ice-ocean variability in the barents sea region: Towards dynamical downscaling. *Ocean Dyn.*, *55*(3-4), 370–387. doi: 10.1007/s10236-005-0008-3

Cheng, A., Casati, B., Tivy, A., Zagon, T., Lemieux, J.-F., & Tremblay, L. B. (2020). Accuracy and inter-analyst agreement of visually estimated sea ice concentrations in canadian ice service ice charts using single-polarization radarsat-2. *The Cryosphere*, *14*, 1289–1310. doi: 10.5194/tc-14-1289-2020

Dukhovskoy, D. S., Ubnoske, J., Blanchard–Wrigglesworth, E., Hiester, H. R., & Proshutinsky, A. (2015). Skill metrics for evaluation and comparison of sea ice models. *J. Geophys. Res.*, *120*, 5910–5931. doi: 10.1002/2015JC010989

Ebert, E. E., & McBride, J. L. (2000). Verification of precipitation in weather systems: determination of systematic errors. *J. Hydrol.*, *239*, 179–202. doi: 10.1016/S0022-1694(00)00343-7

Goessling, H. F., & Jung, T. (2018). A probabilistic verification score for contours: Methodology and application to arctic ice-edge forecasts. *Q. J. R. Meteorol. Soc.*, *144*, 735–743. doi: 10.1002/qj.3242

Goessling, H. F., Tietsche, S., Day, J. J., Hawkins, E., & Jung, T. (2016). Predictability of the arctic sea ice edge. *Geophys. Res. Lett.*, *43*(4), 1642–1650. doi: 10.1002/2015GL067232

Haidvogel, D. B., Arango, H. G., Budgell, P. W., & 17 coauthors. (2008). Ocean forecasting in terrain-following coordinates: Formulation and skill assessment of the regional ocean modeling system. *J. Comp. Phys.*, *227*(7), 3595–3624. doi: 10.1016/j.jcp.2007.06.016

Häkkinen, S., & Mellor, G. L. (1992). Modelling the seasonal variability of a coupled arctic ice-ocean system. *J. Geophys. Res.*, *97*(C12), 20.285–20.304. doi: 10.1029/92JC02037

Hamill, T. M. (2001). Interpretation of rank histograms for verifying ensemble forecasts. *Mon. Wea. Rev.*, *129*(3), 550–560. doi: 10.1175/1520-0493(2001)129⟨0550:IORHFV⟩2.0.CO;2

Hunke, E. C. (2001). Viscous-plastic sea ice dynamics with the evp model: linearization issues. *J. Comput. Phys.*, *170*, 18–38. doi: 10.1006/jcph.2001.6710

Hunke, E. C., & Dukowicz, J. K. (1997). An elastic-viscous-plastic model for sea ice dynamics. *J. Phys. Oceanogr.*, *27*, 1849–1867. doi: 10.1175/1520-0485(1997)027⟨1849:AEVPMF⟩2.0.CO;2

Lavergne, T., Eastwood, S., Teffah, Z., Schyberg, H., & Breivik, L. (2010). Sea ice motion from lowresolution satellite sensors: An alternative method and its validation in the arctic. *J. Geophys. Res.*, *115*(C10032), 14pp. doi: 10.1029/2009JC005958

Leese, J. A., Novak, C. S., & Clark, B. B. (1971). An automated technique for obtaining cloud motion from geosynchronous satellite data using cross correlation. *J. Appl. Meteorol.*, *10*(1), 118–132. doi: 10.1175/1520-0450(1971)010⟨0118:AATFOC⟩2.0.CO;2

Li, Q., Steven, G. P., & Xie, Y. M. (2001). A simple checkerboard suppression algorithm for evolutionary structural optimization. *Struct. Optim.*, *22*(3), 230–239.

doi: 10.1007/s001580100140

Lien, V. S., Gusdal, Y., Albretsen, J., Melsom, A., & Vikebø, F. B. (2013). Evaluation of a nordic seas 4 km numerical ocean model hindcast archive (svim). *Fisken og Havet*, *2013-7*, 80pp.

Mellor, G. L., & Kantha, L. (1989). An iceocean coupled model. *J. Geophys. Res.*, *94*(C8), 10.937–10.954. doi: 10.1029/JC094iC08p10937

Melsom, A., Palerme, C., & Müller, M. (2019). Validation metrics for ice edge position forecasts. *Ocean Science*, *15*(3), 615–630. doi: 10.5194/os-15-615-2019

NCL (2019). The NCAR command language (version 6.6.2) [software]. National Center for Atmospheric Research. Retrieved from `https://ncl.ucar.edu/` doi: 10.5065/D6WD3XH5

Palerme, C., Müller, M., & Melsom, A. (2019). An intercomparison of verification scores for evaluating the sea ice edge position in seasonal forecasts. *Geophys. Res. Lett.*, *46*(9), 4757–4763. doi: 10.1029/2019GL082482

Parkinson, C. L. (2014). Spatially mapped reductions in the length of the arctic sea ice season. *Geophys. Res. Lett.*, *41*(12), 4316–4322. doi: 10.1002/2014GL060434

SVIM (2015). SVIM ocean hindcast archive [data set]. Norwegian Meteorological Institute, Institute of Marine Research. doi: 10.11582/2015.00014

Tokmakian, R., Strub, P. T., & McClean–Padman, J. (1990). Evaluation of the maximum cross-correlation method of estimating sea surface velocities from sequential satellite images. *J. Atmos. Ocean. Tech.*, *7*(6), 852–865. doi: 10.1175/1520-0426(1990)007⟨0852:EOTMCC⟩2.0.CO;2

WMO (2017). Sea-ice information services in the world. *WMO Tech. Rep.*, *574*, 103pp. World Meteorological Organization. Retrieved from `https://nsidc.org/sites/nsidc.org/files/files/noaa/iicwg/2017/WMO_574_Sea_Ice_Information_Services_in_the_World_20170802.pdf`

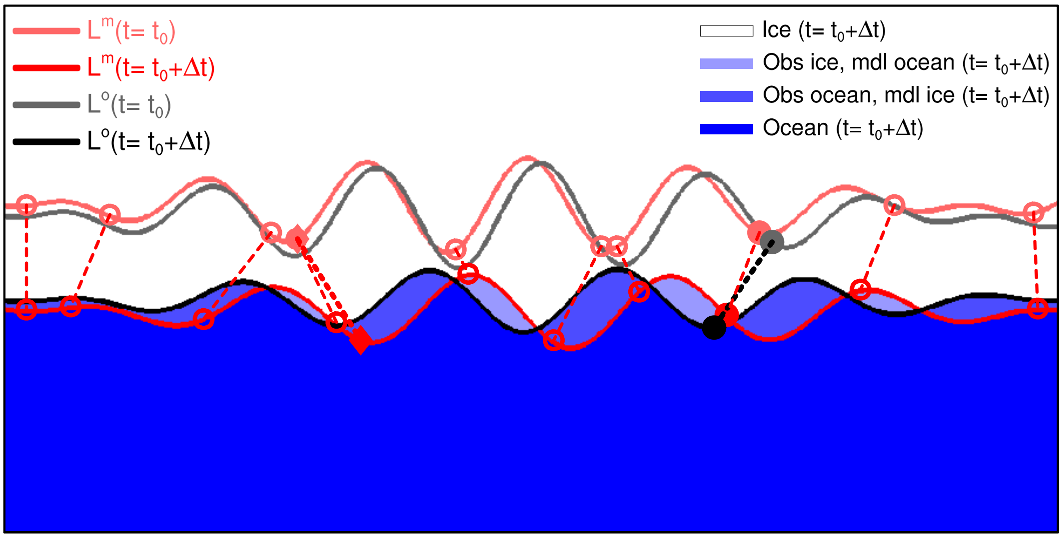


**Figure 1.** Binary fields with values of 1 (ice) and 0 (no ice/ocean) are displayed by white and blue color shading, respectively. Light shades of blue indicate regions with a non-overlapping ice cover, as indicated by the inset color legend. The derived modeled and observed ice edges $L^{(m)}$ and $L^{(o)}$ at $t$=$t_0$+$\Delta t$ are drawn as red and black lines, respectively. The corresponding ice edges that are taken to represent the situation at $t_0$ are drawn as light red and gray curves. The full black circle indicates the position on the observed ice edge at $t_0$+$\Delta t$ which has the largest distance to the ice edge at $t_0$, shown by the full gray circle. The largest displacement of the model ice edge is marked by full diamonds. The full red circle is the position along the model ice edge at $t$=$t_0$+$\Delta t$ closest to the full black circle, while the full light red circle is the position of the observed ice edge at $t_0$ closest to the full red circle. Open circles indicate a random selection of displacement positions for the model results, see the text for details.

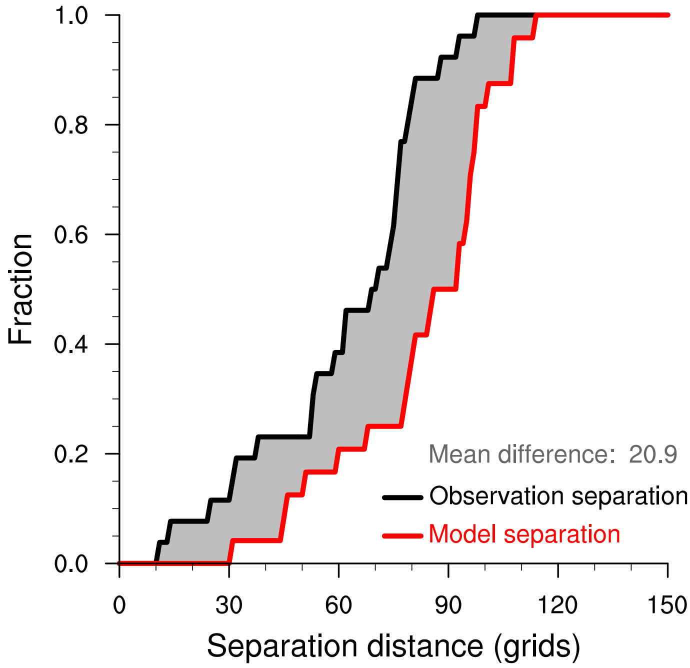


**Figure 2.** Cumulative distributions of the separation (ice edge displacement) distances from $t_0$ to $t_0 + \Delta t$, for model results (red line) and observations (black line). Shown here are results for the idealized example, as displayed in Figure 1, with distances subsampled at intervals of the decorrelation lengths, which are 42 and 38 grid cells along the ice edge for the model results and observations, respectively. The mean separation distance difference is the integral of the area between the curves, here displayed by gray shading. In this case, the mean difference is 20.9 in grid cell units, with larger displacement values in model results than from observations.

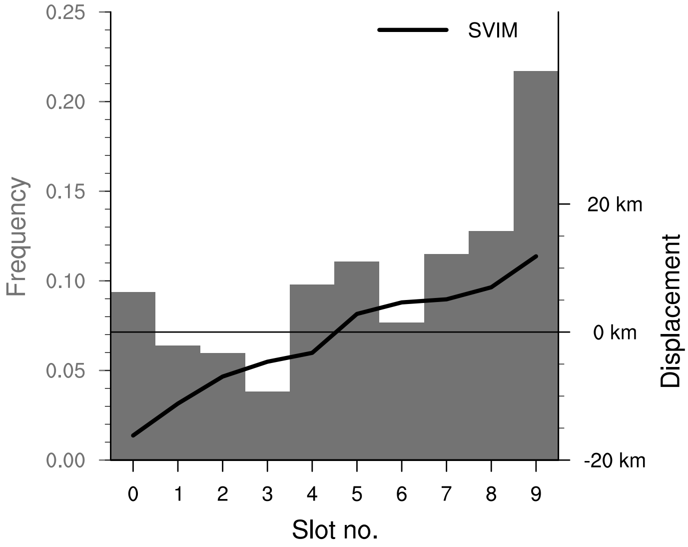


**Figure 3.** Rank histogram for model results for the local ice edge displacement corresponding to the position of the maximum observed displacement. Sets of nine alternative model displacements were derived for each of 235 days with 24 h displacements results. The nine displacement values were ordered from lowest to highest, and the local displacement was given a rank from the slot in which this value belongs, see the text for details. The black curve shows the average local model displacement distances for results belonging to each of the ranks, with negative numbers corresponding to local sea ice retreat in the model results. The average maximum observed displacement is 32 km.

**Table 1.** Category distribution for ice edge displacement distances. Leftmost column gives the displacement distance range for each category, in km. Results from SVIM model simulation and ice chart data are presented separately. Fractions in columns “General” are computed from equation (3), while fractions in columns “OB & C” also take displacements from open boundaries and coasts into account, by replacing $L^{(1)}$ with $\tilde{\bar{L}}^{(1)}$ as defined by equation (16). Results from 354 days of 24h edge displacements have been analyzed, see the text for further details.

| Distance | Fraction of displacements | | | |
|---|---|---|---|---|
| | SVIM results | | ice chart data | |
| | General | OB & C | General | OB & C |
| $< 0$ | 0 | 0 | 0 | 0 |
| 0 – 10 | 0.06 | 0.06 | 0.12 | 0.12 |
| 10 – 20 | 0.28 | 0.29 | 0.06 | 0.08 |
| 20 – 30 | 0.38 | 0.38 | 0.24 | 0.27 |
| 30 – 40 | 0.17 | 0.16 | 0.22 | 0.21 |
| 40 – 50 | 0.06 | 0.06 | 0.15 | 0.14 |
| 50 – 60 | 0.02 | 0.02 | 0.06 | 0.04 |
| 60 – 70 | 0.01 | 0.00 | 0.04 | 0.04 |
| $> 70$ | 0.02 | 0.02 | 0.11 | 0.08 |

**Figure 1.**

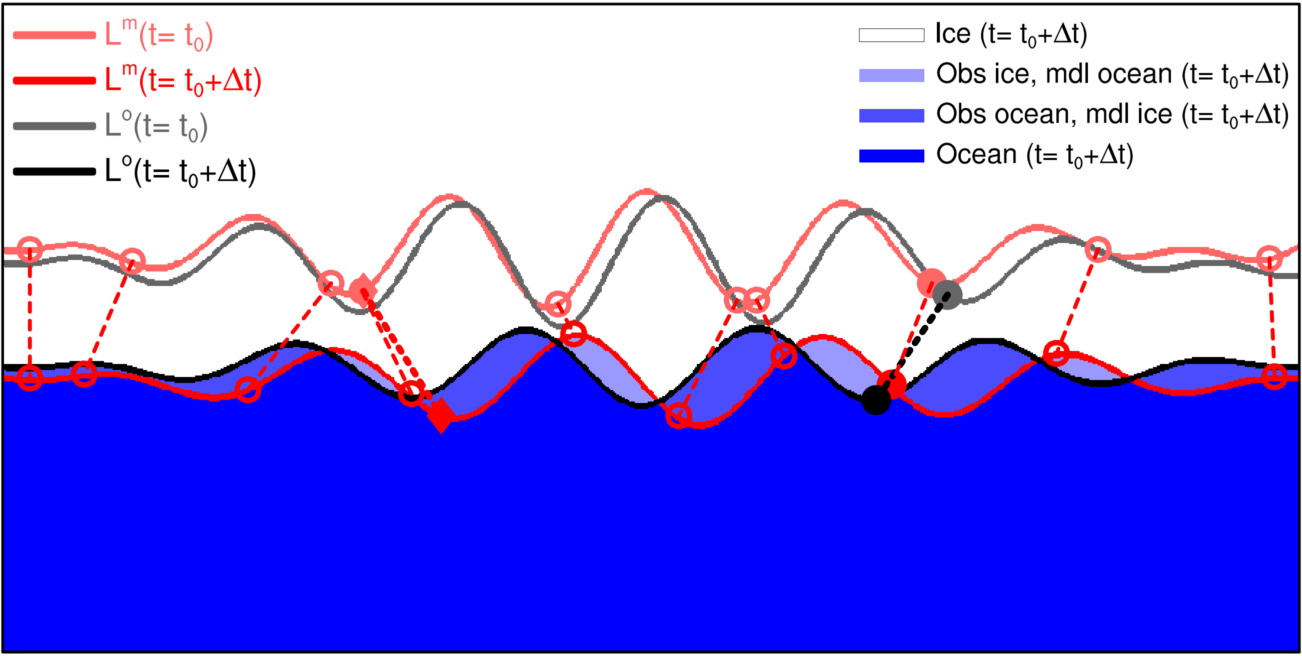

$L^m(t = t_0)$
$L^m(t = t_0+\Delta t)$
$L^o(t = t_0)$
$L^o(t = t_0+\Delta t)$
Ice ($t = t_0+\Delta t$)
Obs ice, mdl ocean ($t = t_0+\Delta t$)
Obs ocean, mdl ice ($t = t_0+\Delta t$)
Ocean ($t = t_0+\Delta t$)

**Figure 2.**

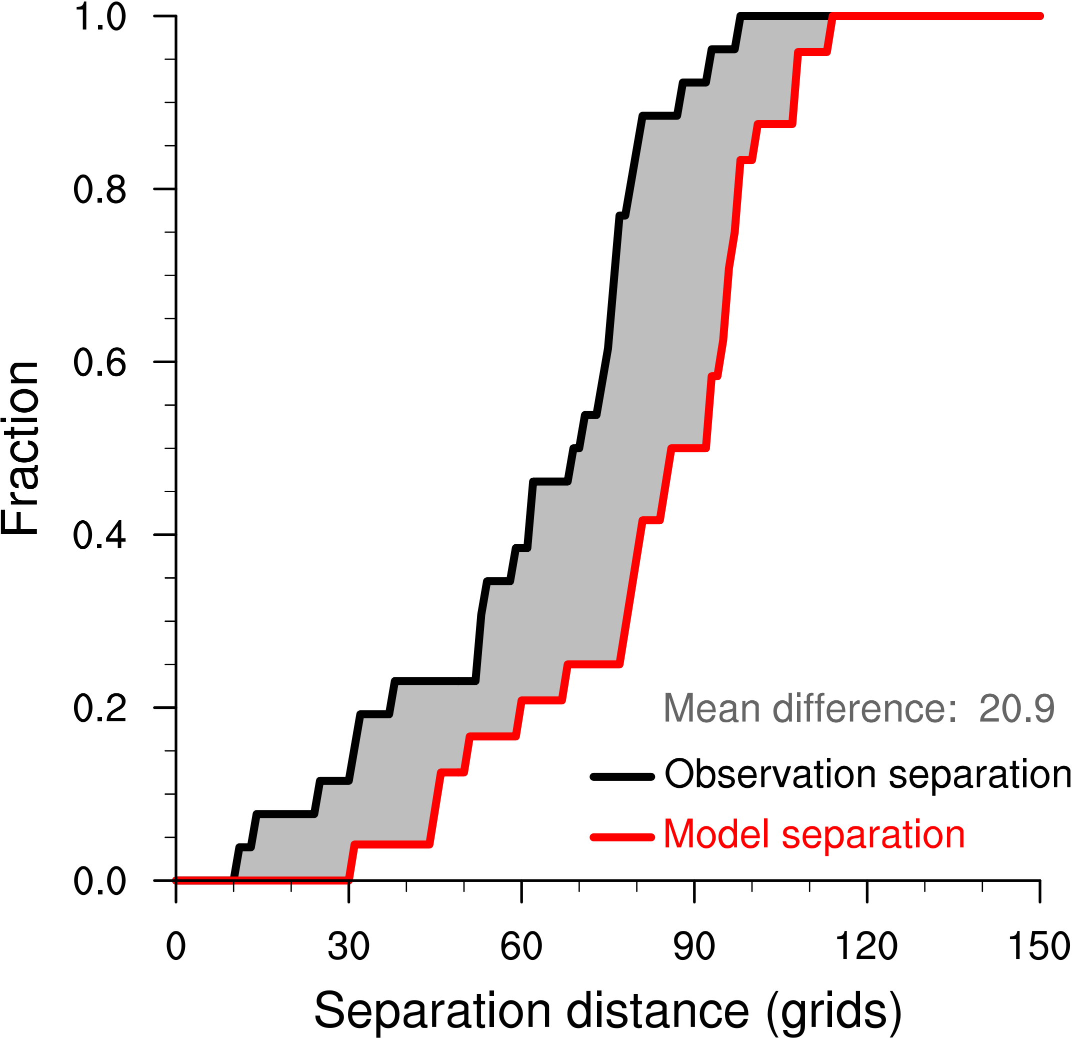

Fraction
1.0
0.8
0.6
0.4
0.2
0.0
0
30
60
90
120
150
Separation distance (grids)
Mean difference: 20.9
Observation separation
Model separation

**Figure 3.**

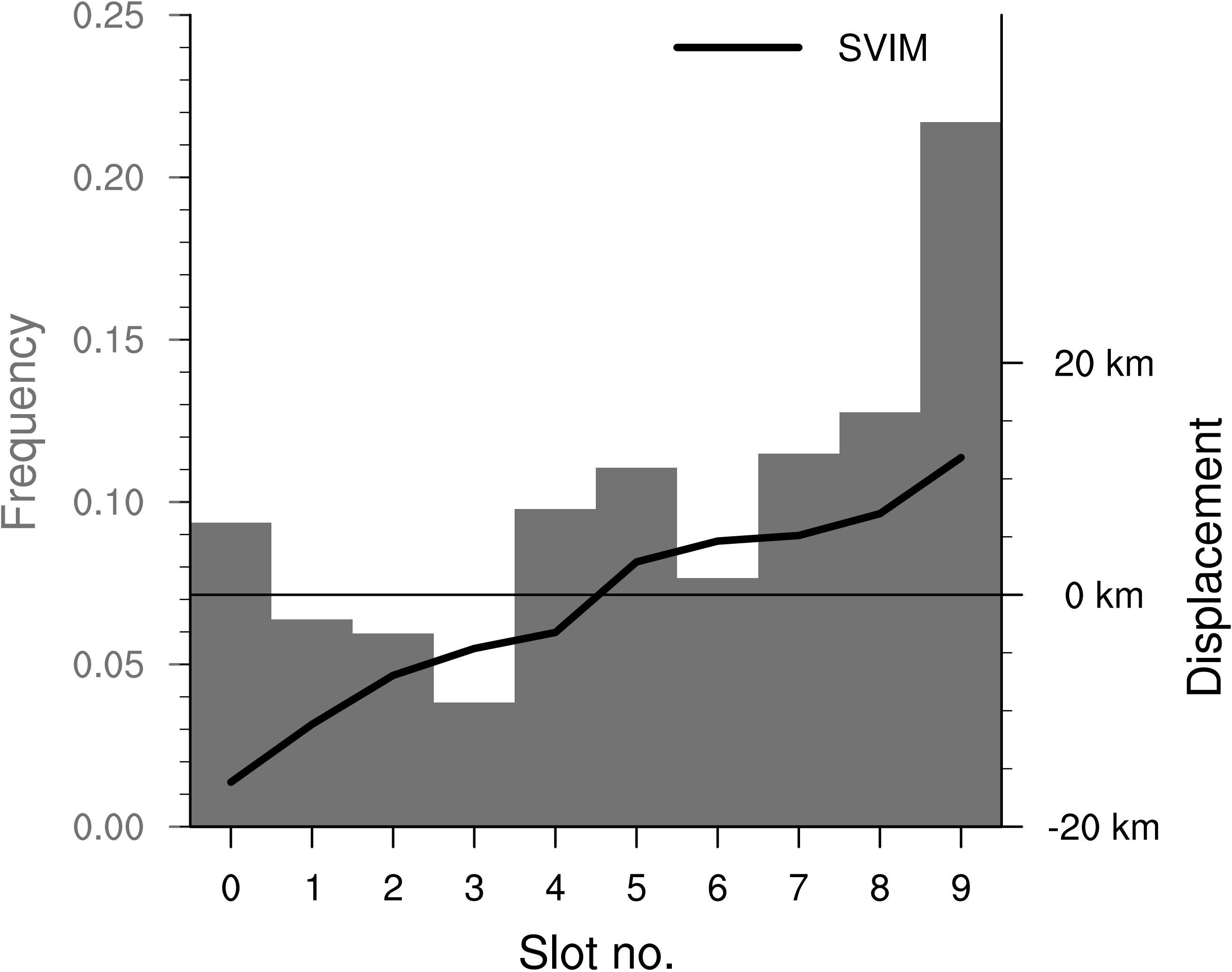
SVIM
Frequency
0.25
0.20
0.15
0.10
0.05
0.00
Displacement
20 km
0 km
-20 km
0
1
2
3
4
5
6
7
8
9
Slot no.